Immersed Boundary Wall-Modelled Large Eddy Simulations of Straight Wings with Three-Dimensional Ice Accretion

Man Long Wong *, Aditya S. Ghate, Gaetan K. W. Kenway, Jordan B. Angel, and Cetin C. Kiris
Volcano Platforms Incorporated, Palo Alto, CA 94304, USA

Wall-Modelled Large Eddy Simulations (WMLES) of flows past two iced straight wings with very different three-dimensional ice shapes accreted at the leading edge are conducted using the *Volcano ScaLES*, which is an octree Cartesian scale-resolving solver with immersed boundary capabilities. Among the two iced straight wing cases chosen, the first one has the streamwise ice shape following the contour of the leading edge, whereas another case has the horn ice features accreted at the leading edge of the airfoil. These two three-dimensional leading edge ice shapes, together with other benchmark iced shapes, were formed on a straight wing with the NACA 23012 airfoil section in the NASA Glenn Icing Research Tunnel and were measured with high-fidelity laser-scanning technique. Aerodynamics of the artificial iced straight wings, manufactured using the laser-scanned geometries, were already measured in dry wind tunnel tests. Using the same laser-scanned models of the two iced wing cases, WMLES are conducted at the chord-based Reynolds number of 1.8 million and Mach number of 0.18 at different angles of attack. The use of the Cartesian grids with the immersed boundary method avoids the labor-intensive process of preparing body-fitted grids for the iced airfoils or wings with highly complex geometry. The in-tunnel setup with the same cross-section as the experimental wind tunnel is recommended and chosen for these WMLES as this allows a more direct comparison of the simulation results with the uncorrected wind tunnel results. In general, the aerodynamic predictions obtained with the in-tunnel computations show good agreement with the experimental measurements, despite the fact that the computational results are affected by some uncertainties due to some assumptions made in the computational tunnel setup.

I. Introduction

The study of the effects of ice accretion on aerodynamic devices is important for the design and development of aircraft. When a wing is contaminated with ice, its aerodynamic performance is significantly degraded due to flow separation triggered by the ice accreted at the leading edge and this leads to concerns of flight safety. Accurate predictions of the impact of ice accretion on the aerodynamic characteristics, such as the maximum lift coefficient, stall angle of attack, and the drag coefficient, etc., using computational methods can speed up and reduce the cost of the design, development, and certification of aircraft under the icing conditions. The Reynolds-Averaged Navier–Stokes (RANS) method was the first Computational Fluid Dynamics (CFD) method employed for the predictions of iced aerodynamics since 90s [1, 2]. In this approach, additional turbulent modelling terms or equations are added to the Navier–Stokes equations for steady or quasi-steady computations. With this turbulence modelling, the need to resolve the turbulent scales is eliminated and simulations can be more affordable with the use of lower resolution grids, or even two-dimensional (2D) grids for 2D iced airfoils. While this approach is cost effective, it tends to over-predict the upper surface pressure, and under-predict the lift coefficient and the stall angle [3–5]. On the other hand, scale-resolving simulations such as the hybrid RANS/Large Eddy Simulations (RANS/LES) or Wall-Modelled Large Eddy Simulations (WMLES) are alternative computational approaches to RANS simulations. In these methods, energy-containing scales are well-resolved while the subgrid-scale (SGS) effects from the small turbulent eddies are modelled. In the hybrid RANS/LES approach, only the inner portion of the boundary layer is modelled with RANS models, whereas Large Eddy Simulation (LES) solutions are obtained in regions of outer boundary layer and flow separation. Compared with the RANS calculations, simulations performed with the hybrid RANS/LES approach generally showed better predictions on the lift and drag coefficients, and the flow features around the ice-accreted airfoils or wings, such as the separation bubbles. These include the numerical studies of iced airfoils or wings using Detached-Eddy Simulations (DES) [6, 7], Delayed Detached Eddy Simulation (DDES) [8], Zonal DES (ZDES) [9], and Dynamic Hybrid RANS/LES method (DHRL) [10]. Recently, there have been some studies on the use of WMLES for iced aerodynamics study [11–14]. In

*Corresponding author.

contrast to the hybrid RANS/LES approach, LES solutions are computed all the way to the walls and the velocity and temperature gradients at the rigid solid boundaries are approximated with modelled shear stress and heat flux boundary conditions [15]. It was reported that the WMLES approach is capable of accurately predicting the flow separation around iced airfoils and the Kelvin–Helmholtz instability (KHI) of the free shear layers induced by the ice [11, 13]. Recently, a literature review of the computational methods for aerodynamic analysis of iced lifting surfaces is provided by Stebbins et al. [16].

Since the starting of NASA's aircraft icing program in 1978 [17], there have been continuous efforts on experimental studies of the ice accretion effects on airfoils and wings [18–24]. The experiments conducted in these works provide valuable data for the assessment of different CFD methods with turbulence modelling for the prediction of iced aerodynamics. Recently, Broeren et al. [23] presented the aerodynamic measurements of a straight wing with the NACA 23012 airfoil section and accretion of different laser-scanned three-dimensional (3D) ice shapes in the dry wind tunnel at the Reynolds number of 1.8 million and Mach number of 0.18. It is confirmed that the laser-scanned iced geometries under different icing conditions can accurately reproduce the small-scale ice features of the original ice shapes. These laser-scanned 3D ice geometries and the aerodynamic measurements from the wind tunnel provide high-fidelity test data for the validation of CFD methods and turbulence models. These test cases have already been used for the assessment of the lattice-Boltzmann method with hybrid RANS/LES [25] and unstructured Voronoi Navier–Stokes method with WMLES [14].

In this work, a state-of-the-art octree Cartesian Navier–Stokes Graphics Processing Unit (GPU)-accelerated solver, Volcano ScaLES, is used for conducting WMLES of the flows around two iced straight wing cases with the NACA 23012 airfoil section in [23]. The two iced straight wings have very different ice features accreted at the leading edges, which are generally classified as the streamwise ice and horn ice cases based on the aerodynamic classification described by Bragg et al. [26]. With the use of the Cartesian method, the labor cost and computational expense to prepare the computational mesh are largely reduced for problems with very complex geometries such as the iced straight wing cases in this work, while high accuracy of the numerical methods can still be maintained since the grid cells remain isotropic near walls. Although the grid cells do not align with the geometry, accurate wall-stress boundary conditions are still applied at the complex ice geometry using an immersed boundary method with the WMLES approach. By comparing the simulation results with the experiments data, the capability of the CFD solver in predicting the iced aerodynamics of the two benchmark iced wing cases are examined in details.

II. Description of Problems

Flows past two iced straight wings with the same NACA 23012 airfoil section but different types of 3D leading edge ice accretions are considered in this work. These two ice accretion cases, labelled as ED1977 and ED1978, are adopted from the six iced straight wing cases presented in the experimental work by Broeren et al. [23]. The 3D ice shapes formed at the leading edge of the NACA 23012 airfoil section were extracted with high fidelity laser scanning in the NASA Glenn Icing Research Tunnel. Artificial iced leading edges were fabricated using the Rapid Prototype Manufacturing (RPM) with the laser-scanned geometries, which were then attached to the leading edge of a straight wing test model with the NACA 23012 airfoil section for aerodynamic measurements in the University of Illinois wind tunnel. The test model has a chord length of $c = 0.4572$ m (18 in) and the wind tunnel of the University of Illinois has a test section of 0.85344 m (33.6 in) by 1.2192 m (48 in), where the straight wing has a span of $b = 0.85344$ m (with aspect ratio, AR = 1.87). These iced straight wing cases were tested at the chord-based Reynolds number of $Re = 1.8 \times 10^6$ and Mach number of $M = 0.18$. The ED1977 case has the streamwise ice shape which is characterized by the ice shape conformal to the leading edge of the airfoil section. This ice shape was reported to be formed under the rime ice conditions. As seen from the 2D section cut in Figure 1(a), the rime ice feathers also extend farther downstream and are relatively large (compared to another streamwise case ED1966 in [23]) due to large water drop size (median volumetric diameter, MVD = 30 μm) used in the icing wind tunnel. On the other hand, the ED1978 case is formed by a typical glaze ice accretion. As shown in Figure 1(b), the leading edge of the airfoil section is accreted with large horns on both upper and lower surfaces. The 3D computational model with the leading edge 3D ice accretions for both cases are shown in Figure 2.

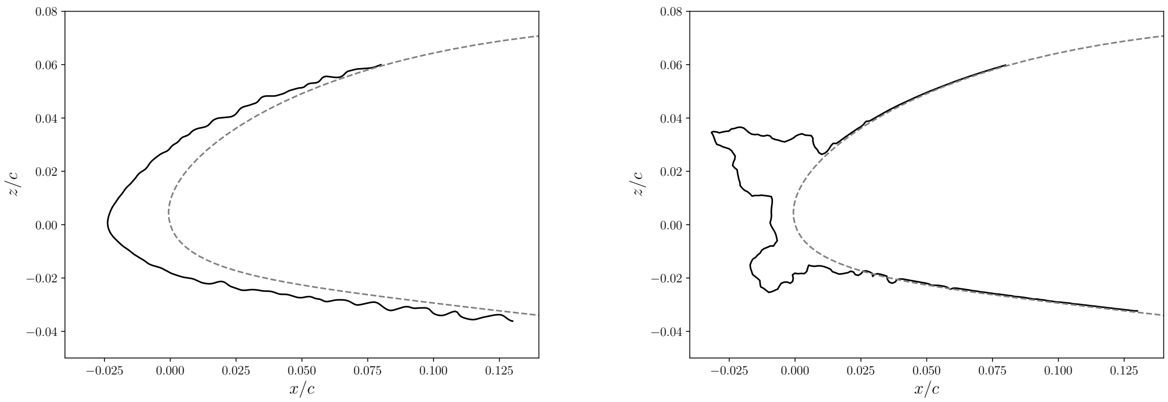

(a) ED1977 (b) ED1978

Fig. 1 2D section cuts of the ED1977 and ED1978 ice accretion cases [23]. Solid line: ice accretion; dashed line: clean NACA 23012 airfoil section.

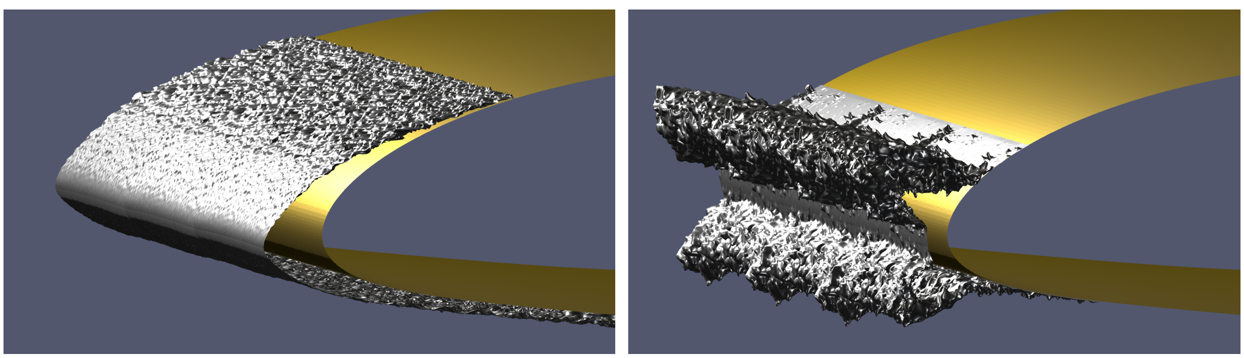

(a) ED1977 (b) ED1978

Fig. 2 3D iced geometries of the ED1977 and ED1978 cases. The laser-scanned surface mesh and the clean NACA 23012 surface are colored in silver and gold respectively.

III. Details of Simulations

A. Numerical Methods

The scale-resolving CFD solver, Volcano ScaLES, is used for performing the LES of the iced straight wings. The solver is based on the compressible Navier–Stokes equations where the inviscid flux is discretized with a fourth order finite difference scheme with the favorable kinetic energy and entropy consistency properties. The viscous flux discretization consists of a mix of four order and second order finite differencing that has improved resolution and robustness for high Reynolds number turbulent flow. As a result, there is no need to apply numerical dissipation through the inviscid flux operator for numerical stability for turbulent flows. The overall numerical scheme has minimum dissipation in turbulence regions, with the use of physics-based flow sensors. Additional methods to reduce generation of spurious numerical noise at walls as well as at coarse-fine grid interfaces are also utilized in the present work. The Cartesian gridding with unit aspect ratio is beneficial for the use of explicit time-stepping scheme even in flows involving highly complex geometries as the perfectly isotropic grid cells near the geometry do not introduce any numerical stiffness associated with complex grid topologies. The time integration is performed using the explicit third order strong-stability-preserving Runge–Kutta time stepping scheme [27].

Geometries are represented in the computations using a sharp immersed boundary method capable of enforcing inviscid no-penetration boundary conditions as well as viscous skin friction with appropriate Reynolds number asymptotic properties using an equilibrium wall model. In this WMLES approach, only the outer boundary layer eddies are resolved while the subgrid eddies in the inner boundary layer are modelled with the wall model. This largely eliminates the need to resolve the turbulent boundary layer using very fine grid cells and reduce the computational expenses. The wall model that provides a wall shear stress constraint uses solution information interpolated via probing at a fixed distance of $3\Delta/2$ into the fluid away from walls, where Δ is the local grid spacing. All simulations presented in this work utilize the Smagorinsky subgrid scale (SGS) model with dynamic procedure [28, 29] and a constant turbulent Prandtl number to model the subgrid scales.

The CFD solver has been validated using a sequence of WMLES including: a) F-16XL aircraft aerodynamics [30], b) automotive aerodynamics [31], c) subsonic jets [32], d) airframe noise [33], and e) vibro-acoustics of a launch vehicle [34].

B. Computational Architecture

Motivated by the need to fully exploit all available resources on modern GPUs, Volcano ScaLES is written exclusively in C++ and CUDA. On simulations involving non-canonical geometries such as those considered in this paper, we achieve approximately 30% of peak FLOPs on compute-oriented devices along with nearly perfect (> 95%) weak scaling efficiency from 1 to 8 GPUs. Unlike most CFD codes, the majority of the computations are compute bound and we achieve high performance even in graphics-oriented, bandwidth-restricted devices, such as the Nvidia GeForce RTX 4090. The combination of Cartesian methods and an explicit time stepping scheme yields extremely low memory requirements: ScaLES can simulate between 8.5 and 10 million cells per gigabyte of GPU memory depending on the complexity of the configuration. Simulations containing between 400 and 500 million cells are routinely performed on desktop computers containing just two RTX 4090 GPUs with 24 GB of memory each.

C. Problem Setup

All simulations of the full span iced wings are conducted in a closed domain similar to the actual wind tunnel, where $x = c/4$ is defined as the rotation center of the wind tunnel and is also the quarter chord location of the clean or iced wings. While the actual wind tunnel of the University of Illinois has slightly diverging walls, a rectangular tube with a constant cross-section of 0.85344 m × 1.2192 m and a length of 9.7536 m (384 in) is used as the test section in the simulations. A contraction with the inlet boundary is attached upstream to the test section at $x = -3.5433$ m (-139.5 in) to facilitate the setup of the numerical wind tunnel. The setup of the numerical model of the wind tunnel with the ED1978 wing is shown in Figure 3. All wind tunnel walls are approximated as slip and adiabatic walls. In the wind tunnel tests, non-dimensionalization of the aerodynamic quantities are performed using the reference quantities such as the static and dynamic pressure values, p_∞ and q_∞, measured at a location 48 in upstream of the iced wing. In order to set up the numerical wind tunnel that is as close as the actual wind tunnel, the back pressure at the outlet boundary of the test section is first tuned iteratively using a precursor simulation with a lower grid resolution (grid A) such that the Mach number and dynamic pressure at a point probe located 1.2192 m (48 in) upstream of the quarter chord location of the airfoil section are similar to the corresponding reference values ($M = 0.18$ and $q_\infty = 2268.0$ Pa respectively). Note that this procedure needs to be carried out independently at each angle of attack for each iced straight wing case. This process to setup the wind tunnel is different than that in [25] where the reference values are directly measured at the upstream location in their simulations to correct the non-dimensionalization of the aerodynamic quantities. We believe our approach can provide a more direct comparison between the results of the simulations and the experiments, as the Mach and Reynolds numbers are the primary problem parameters specified for the test cases. While only a back pressure value is required for the outlet, stagnation pressure and temperature boundary conditions are prescribed at the inlet using the problem Mach number and the target static pressure and temperature at the point probe. In order to prevent the reflection of acoustic waves at the inlet and outlet, acoustic sponges with increased viscosity are added in regions far away from the iced wings ($x < -3.5433$ m or $x > 22.860$ m).

Five angles of attack at $\alpha = 5.989°$, $7.988°$, $9.979°$, $12.004°$, and $14.000°$ are chosen for the ED1977 case, while four angles of attack at $\alpha = 2.000°$, $3.995°$, $5.992°$, and $7.996°$ are simulated for the ED1978 case. During the setup of the simulations at various angles of attack, the wind tunnel is rotated using the corresponding angles while the chord of the iced wing is still aligned with the x-direction. After the computational domain is prepared, Cartesian grids inside the numerical wind tunnel around the iced wings are generated automatically using a recursive octree approach with the Volcano meshing software. Grids around practical configurations consist of unstructured grids of millions of "boxes" each of which contains a structured grid of 4^3 or 8^3 cells. This method gives nearly all the computational advantages of

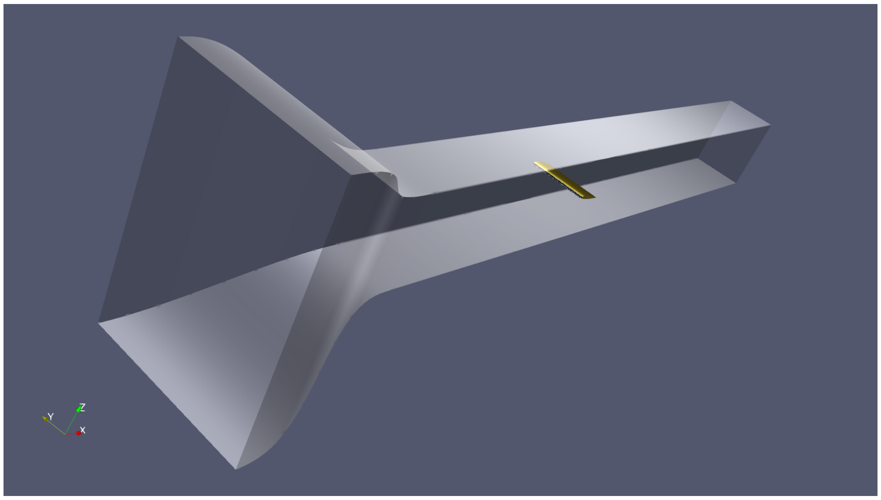

Fig. 3 Wind tunnel setup at α = 7.996° with a full span ED1978 iced straight wing in the test section.

structured grids while retaining the ability to closely follow surfaces and minimize the number of "dead" cells inside the geometry. Typically, 90-95% of the total cells in a grid are compute cells, while the remaining ones are considered "dead" or "blanked" cells. The generated grid is composed of meshes at different mesh levels, where the refinement ratio is 1:2 in each direction across successive mesh levels.

Four different grids, labelled as grids A, C, D, and E, are designed for the ED1977 streamwise ice case. The grid A has five levels of meshes where the finest level has a grid spacing of 1.79 mm which is equivalent to 256 points per chord length. The regions near the iced airfoil surface are refined to the finest level with a thickness height of eight grid cells. The base mesh has a grid spacing of 28.575 mm which covers most of the regions of the numerical wind tunnel except regions near the wind tunnel walls and the iced wing which are one mesh level finer. Grids C and D have two and three more levels of grid refinement near the airfoil surface over grid A where the finest grid spacings are 0.446 mm and 0.223 mm respectively, which are equivalent to 1024 and 2048 points per chord length respectively. For both grids, a large region on the suction surface of the wing has the thickness height maintained to be 7.14 mm for the finest mesh (16 and 32 cells for grids C and D respectively), while the thickness height is set at eight grid cells in other regions near the wing and wind tunnel walls. Finally, grid E has one more level of local mesh refinement in regions near the iced leading edge which is expected to resolve the complex and small-scale accreted ice features better. The grids C, D, and E for the ED1977 case are illustrated in Figure 4. Three different grids, grids A, C, and D, are also employed for the simulations of the horn ice ED1978 case. The design of grid A for ED1978 case are similar to that for ED1977 case. Grid C has two more levels of grid refinement near the wing surface where the finest grid spacing is 0.446 mm which is equivalent to 1024 points per chord length while the thickness height of the finest mesh around the airfoil section is set to be eight grid cells. In addition, there is large volume refinement near the upper and lower ice horns to better resolve the horn ice geometry and capture the growth of the shear instabilities induced by the horn ice, as well as the flow transition to turbulence and the separation bubbles. Grid D is similar to grid C but has one more level of grid refinement over the grid C near the leading edge of the iced wing to improve the predictions of the KHI at the shear layers and the transition to turbulence. For all of these grids, the regions near the clean portion of the airfoil surface are maintained at a thickness height of eight grid cells. The grids C and D for the ED1978 case are shown in Figure 5.

As mentioned previously, there is a precursor simulation with grid A at each angle of attack for the iced wing cases. These simulations with grid A, which are computationally more affordable than any simulations with higher resolution grids (grids C, D, or E), are used for tuning the back pressure at the outlet boundary such that the problem parameters are achieved at the point probe upstream of the wings. These grid A simulations are initialized with uniform flows at freestream Mach number, $M = 0.18$, and freestream temperature, $T_\infty = 300.97$ K, and are run for 400 convective time units (CTUs) to flush out transient, where one CTU is defined as c/U_∞, with U_∞ being the freestream velocity magnitude used in the initial conditions. The simulations with higher resolution grids are initialized using the interpolated solutions from the solutions of the corresponding grid A simulations at 400th CTU. Since the computations with grid A mainly serve for setting up the outflow boundary conditions and the initial conditions for the higher resolution simulations, the results with grid A will be excluded in the discussion section of this work. The details of the simulations including

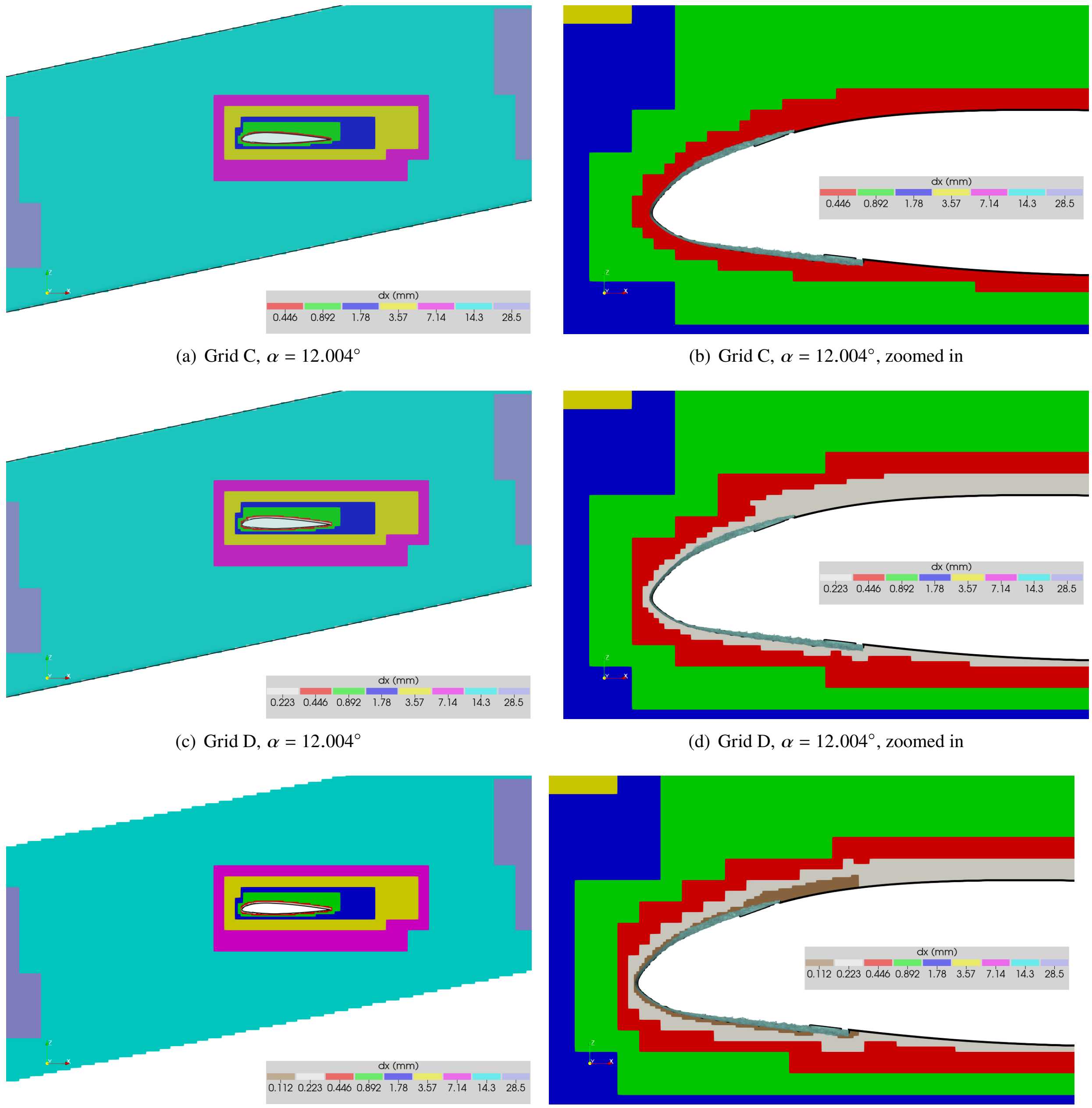

(a) Grid C, $\alpha = 12.004°$ (b) Grid C, $\alpha = 12.004°$, zoomed in

(c) Grid D, $\alpha = 12.004°$ (d) Grid D, $\alpha = 12.004°$, zoomed in

(e) Grid E, $\alpha = 12.004°$ (f) Grid E, $\alpha = 12.004°$, zoomed in

Fig. 4 Cross-section of the computational grids at the center-plane showing the grid topologies with grid spacings for the ED1977 simulations. The black and thick contour line represents the section cut of the iced straight wing. The blue translucent surface shows the 3D ice geometry.

the grid statistics and the computational resources used are shown in Tables 1 and 2 respectively for the ED1977 and ED1978 simulations respectively.

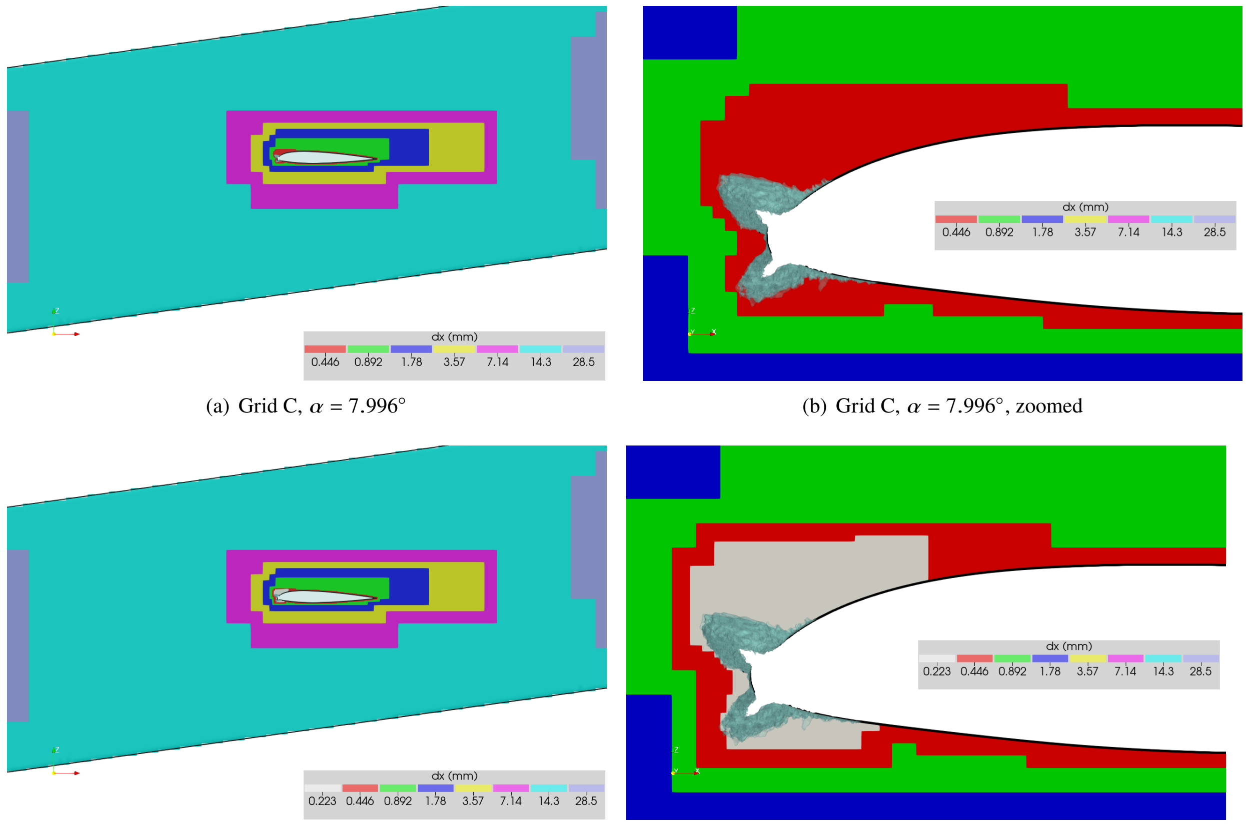

(a) Grid C, α = 7.996°

(b) Grid C, α = 7.996°, zoomed

(c) Grid D, α = 7.996°

(d) Grid D, α = 7.996°, zoomed

Fig. 5 Cross-section of the computational grids at the center-plane showing the grid topologies with grid spacings for the ED1978 simulations. The black and thick contour line represents the section cut of the iced straight wing. The blue translucent surface shows the 3D ice geometry.

Angle of attack	Grid label	Minimum grid spacing (mm)	Number of compute grid cells (million)	Averaged time step size (μs)	Number of CTUs	Number of GPUs used	Wall-clock hours per 10 CTUs
5.989°	A	1.786	21.40	3.021	400	2 x GeForce RTX 4090	0.051
	C	0.446	142.65	0.736	20	2 x GeForce RTX 4090	2.364
	D	0.223	589.99	0.357	20	6 x GeForce RTX 4090	5.271
7.988°	A	1.786	22.34	2.960	400	2 x GeForce RTX 4090	0.057
	C	0.446	144.70	0.729	20	2 x GeForce RTX 4090	2.402
	D	0.223	592.78	0.352	20	6 x GeForce RTX 4090	5.449
9.979°	A	1.786	24.44	2.941	400	2 x GeForce RTX 4090	0.065
	C	0.446	145.39	0.718	20	2 x GeForce RTX 4090	2.436
	D	0.223	594.03	0.348	20	6 x GeForce RTX 4090	5.561
	E	0.112	831.21	0.169	20	6 x GeForce RTX 4090	16.12
12.004°	A	1.786	22.39	2.886	400	2 x GeForce RTX 4090	0.065
	C	0.446	142.40	0.706	45	2 x GeForce RTX 4090	2.474
	D	0.223	587.45	0.345	45	6 x GeForce RTX 4090	5.625
	E	0.112	826.57	0.169	45	6 x GeForce RTX 4090	16.42
14.000°	A	1.786	23.36	2.858	400	2 x GeForce RTX 4090	0.059
	C	0.446	146.62	0.702	45	2 x GeForce RTX 4090	2.611

Table 1 Details of the ED1977 simulations.

Angle of attack	Grid label	Minimum grid spacing (mm)	Number of compute grid cells (million)	Averaged time step size (μs)	Number of CTUs	Number of GPUs used	Wall-clock hours per 10 CTUs
2.000°	A	1.786	22.77	2.948	400	2 x GeForce RTX 4090	0.056
	C	0.446	141.23	0.712	50	2 x GeForce RTX 4090	1.417
	D	0.223	287.92	0.351	50	2 x GeForce RTX 4090	5.214
3.995°	A	1.786	22.87	2.933	400	2 x GeForce RTX 4090	0.054
	C	0.446	141.19	0.703	50	2 x GeForce RTX 4090	1.383
	D	0.223	285.53	0.346	50	7 x GeForce RTX 4090	2.019
5.992°	A	1.786	21.50	2.905	400	2 x GeForce RTX 4090	0.055
	C	0.446	140.44	0.698	50	2 x GeForce RTX 4090	1.418
	D	0.223	282.45	0.346	50	7 x GeForce RTX 4090	1.971
7.996°	A	1.786	22.46	2.894	400	2 x GeForce RTX 4090	0.057
	C	0.446	144.02	0.703	200	2 x GeForce RTX 4090	1.427
	D	0.223	285.99	0.344	200	7 x GeForce RTX 4090	1.964

Table 2 Details of the ED1978 simulations.

IV. Computational Results and Discussions

A. Flow Visualizations

The iso-surfaces of Q-criterion from the WMLES for the cases ED1977 and ED1978 at different angles of attack are shown in Figures 6 and 7 respectively. The Q-criterion is normalized by the CTU and is colored by the streamwise velocity component normalized by U_∞. In addition, the instantaneous streamwise velocity component contours, normalized by U_∞, near the leading edge for the two cases are shown in Figures 8 and 9 at the center-plane. For the case ED1977, the boundary layers transition to turbulent flows near the leading edge already at all angles due to the tripping effect caused by the complex 3D ice accreted at the leading edge. This can also be seen from the streamwise component of the skin friction coefficient on the surface of the wing and the streamwise velocity contours near the leading edge. While the boundary layer is still attached on the entire suction side at α = 5.989°, 7.988°, and 9.979°, flow separation happens from the mid-chord location at α = 12.004° and the wing stalls. As for the case ED1978, large flow separations are shown at both upper and lower horns of the iced wing at all angles of attack, where shear layers are formed. At the shear layers, rapid roll-up occurs due to KHI and transition to turbulence happens quickly downstream of the horns. At all angles, the turbulent shear layers on both suction and pressure sides reattach and form separation bubbles with flow reversal, which can be seen from the streamwise velocity component. But the length of the separation bubble increases with the α. The boundary layer becomes fully turbulent after the reattachment of the separation bubble. While the turbulent boundary layers are still fully attached on the suction side at α = 2.000° and 3.995°, it starts to separate at α = 5.992°. At α = 12.004°, the boundary layer is largely separated on the suction side, which can also be seen from the plot of the streamwise component of skin friction coefficient.

B. ED1977 Case

The time histories of the coefficients of lift (C_L), drag (C_D), and pitching moment (C_M) of the ED1977 iced wing from some of the simulations are shown in Figure 10. From the plot, it can be seen that even when the flows are initialized from the solutions of the precursor simulations using grid A, these coefficients still have some levels of fluctuations initially. However, most of these aerodynamic quantities are quite well converged shortly after 10 CTUs with minor variations in time. Ignoring α = 12.004° and 14.000°, all of these simulations are run until the 20th CTU where the statistics are collected from the 15th CTU. At α = 12.004, while the aerodynamic coefficients obtained with grid E seem to be quite stationary for a short period of time after the initial transient, they change over time with quite large variations even after 20 CTUs. This behaviour is similar for the simulation with grid C at α = 14.000°. Therefore, we decide to delay the sampling start time to the 30th CTU for all computations at these two high angles of attack and also extend these simulations until the 45th CTU.

The mean (time-averaged) values and fluctuations of the aerodynamic coefficients against the angle of attack for the ED1977 case is shown in Figure 11. In these plots, the fluctuations are measured using root mean squares (RMSs) which are shown as error bars above the mean values. In addition, the experimental results for the clean wing is also included to show the detrimental effects caused by the leading edge ice accretion on the aerodynamics performance.

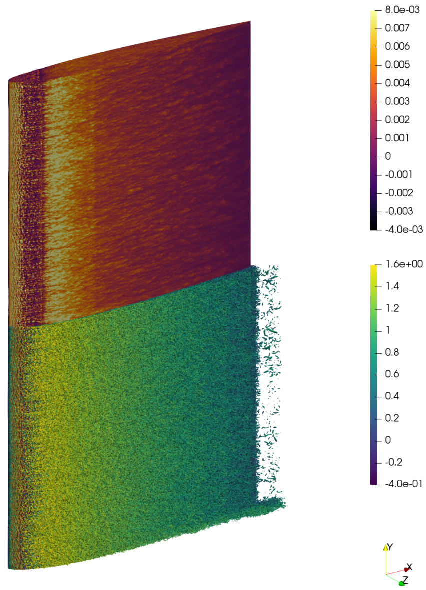

(a) α = 5.989° (grid D)

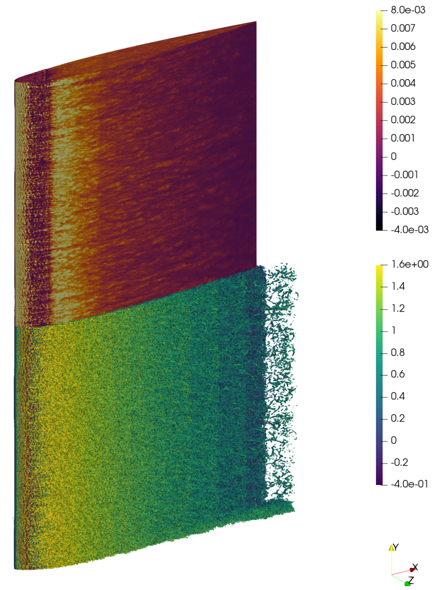

(b) α = 7.988° (grid D)

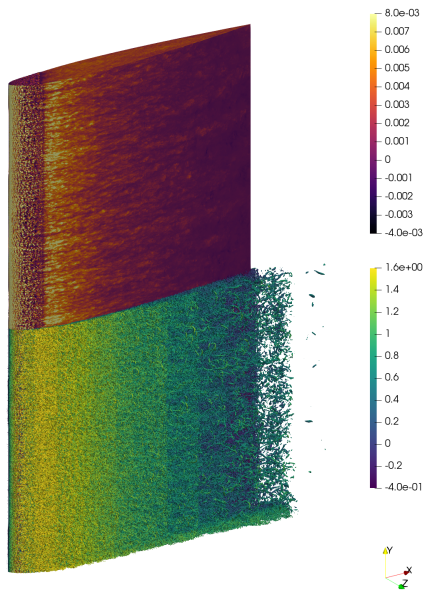

(c) α = 9.979° (grid E)

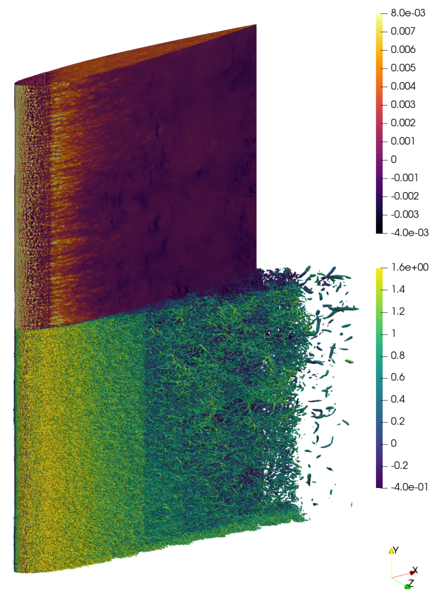

(d) α = 12.004° (grid E)

Fig. 6 Iso-surfaces of the Q-criterion normalized by the convective time unit, CTU, at the value of 2000, colored by the streamwise velocity component normalized by the freestream velocity magnitude, U_∞, at different angles of attack, α, on the suction side of the iced wing for the ED1977 case. Iso-surfaces are only shown on the bottom half of the wing. The surfaces of the iced wings are colored by the streamwise component of the skin friction coefficient.

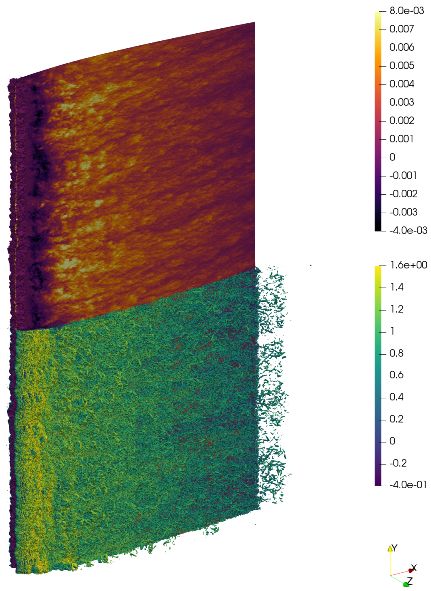

(a) α = 2.000° (grid D)

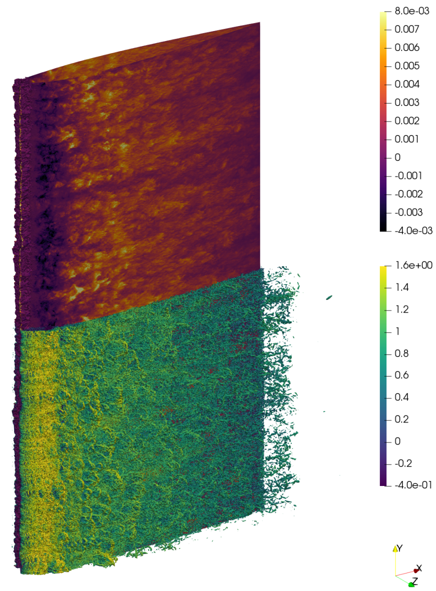

(b) α = 3.995° (grid D)

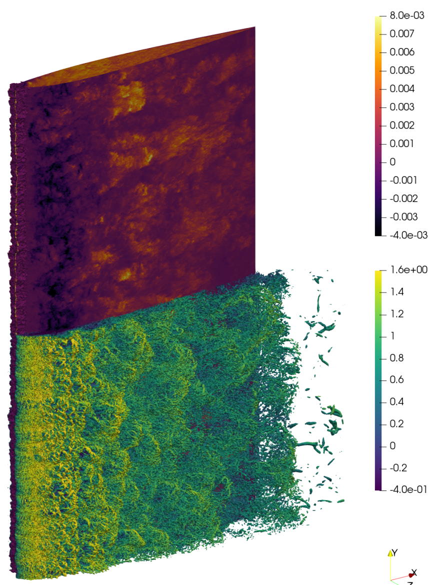

(c) α = 5.992° (grid D)

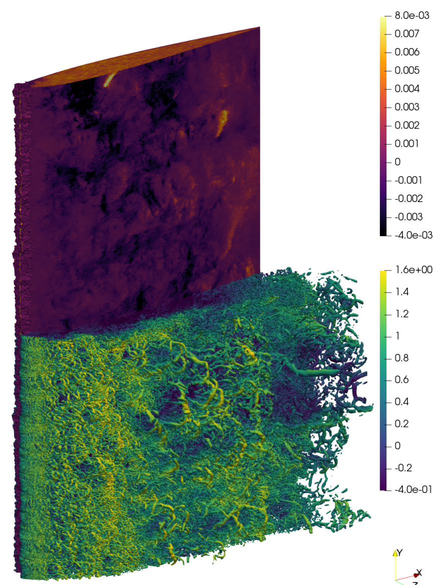

(d) α = 7.996° (grid D)

Fig. 7 Iso-surfaces of the Q-criterion normalized by the convective time unit, CTU, at the value of 1000, colored by the streamwise velocity component normalized by the freestream velocity magnitude, U_∞, at different angles of attack, α, on the suction side of the iced wing for the ED1978 case. Iso-surfaces are only shown on the bottom half of the wing. The surfaces of the iced wings are colored by the streamwise component of the skin friction coefficient.

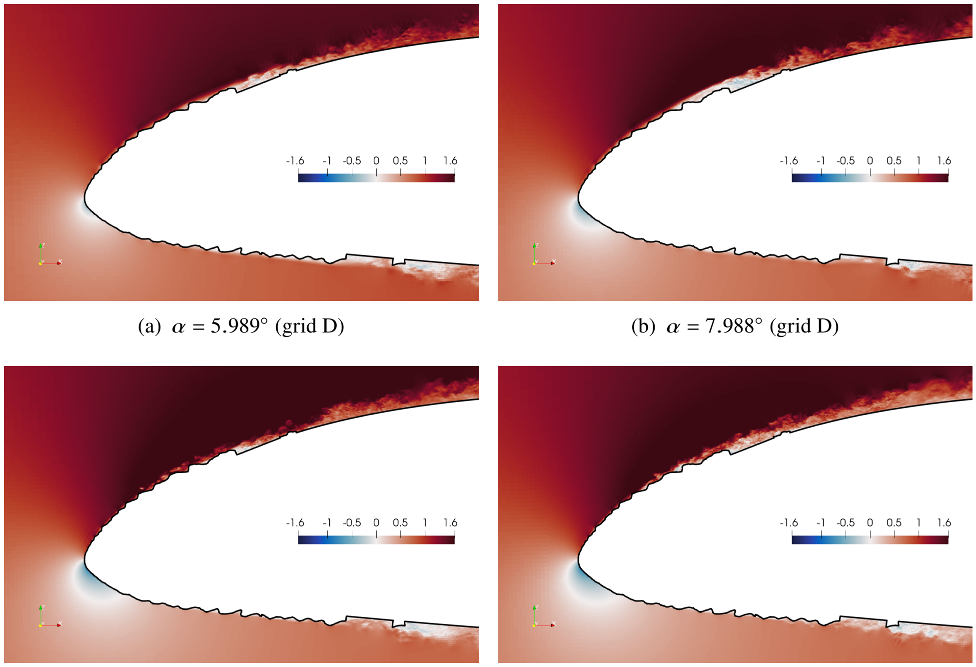

(a) α = 5.989° (grid D)

(b) α = 7.988° (grid D)

(c) α = 9.979° (grid E)

(d) α = 12.004° (grid E)

Fig. 8 Instantaneous streamwise velocity component normalized by the freestream velocity magnitude, U_∞, at different angles of attack, α, at the center-plane for the ED1977 case.

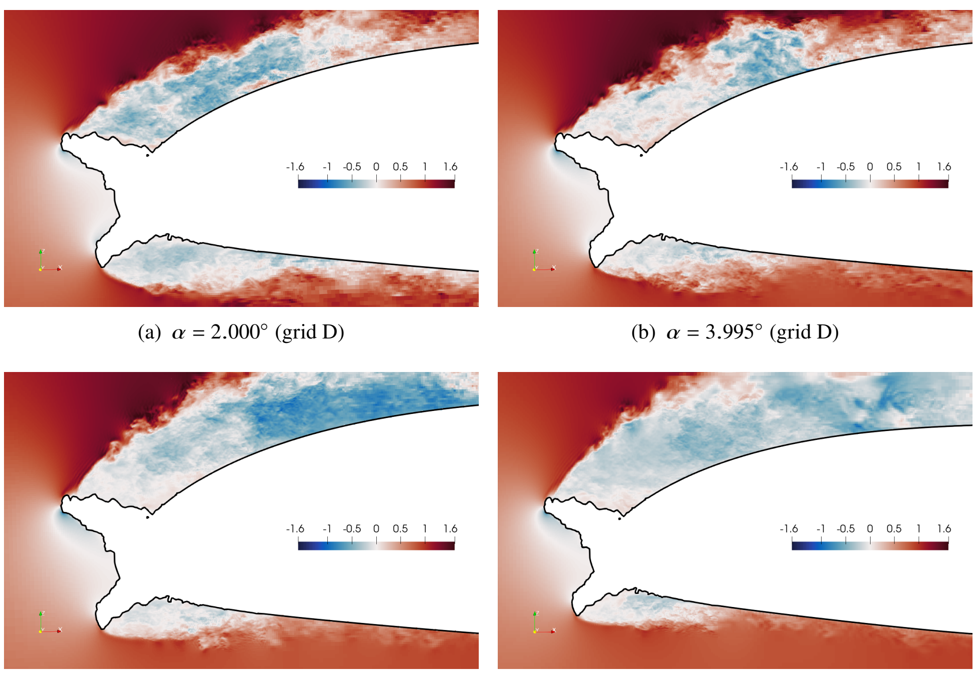

(a) α = 2.000° (grid D)

(b) α = 3.995° (grid D)

(c) α = 5.992° (grid D)

(d) α = 7.996° (grid D)

Fig. 9 Instantaneous streamwise velocity component normalized by the freestream velocity magnitude, U_∞, at different angles of attack, α, at the center-plane for the ED1978 case.

From the experimental results, it can be seen that with the accretion of the streamwise ice at the leading edge of the

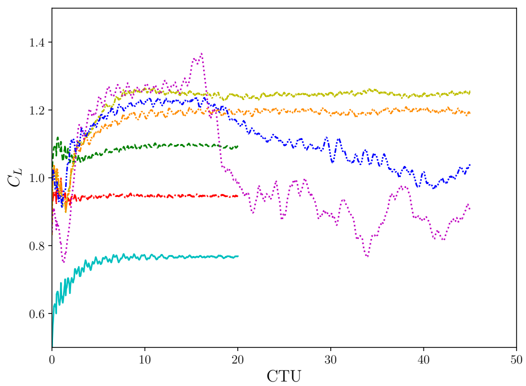

(a) Lift coefficient

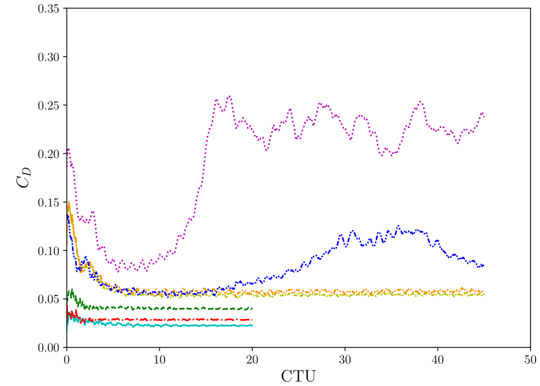

(b) Drag coefficient

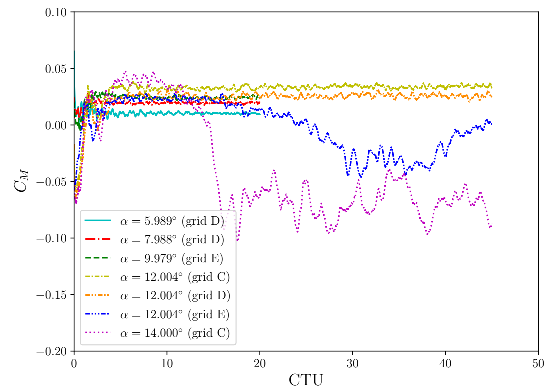

(c) Pitching moment coefficient

Fig. 10 Time histories of the lift, drag, and pitching moment coefficients from the simulations at different angles of attack, α, for the ED1977 case. Cyan solid line: α = 5.989° with grid D; red loosely dash-dotted line: α = 7.988° with grid D; green dashed line: α = 9.979° with grid E; yellow densely dash-dotted line: α = 12.004° with grid C; orange densely dash-dot-dotted line: α = 12.004° with grid D; blue densely dash-triple-dotted line: α = 12.004° with grid E; magenta dotted line: α = 14.000° with grid C.

NACA23012 airfoil section, the maximum lift coefficient is reduced to $C_{L,max}$ = 1.04 from 1.49, while the stall angle of attack decreases to α_{stall} = 11.3° from 14.4°. In addition, the drag coefficient C_D is largely increased while the slope of the pitching moment coefficient C_M is more positive from small angles of attack until the stall angle for the iced wing. The plot of lift coefficient shows that the grid sensitivities of the mean lift coefficient are small at the three lower angles of attack, α = 5.989°, 7.988°, and 9.979°. The RMSs of the fluctuations in the aerodynamic coefficients are also small at these angles. In general, these computational predictions on C_L agree well with the experimental measurements using force balance. At α = 12.004° which is larger than the stall angle, quite large grid sensitivity can be seen. When the grid is refined from grids C to E, there is an improvement in C_L from the computations towards the experimental results. While over-predictions in mean C_L are observed with grids C and D, the C_L obtained with grid E has the mean value close to the experimental one but also shows much larger RMS of the fluctuation. In general, the α_{stall} is predicted to be in between α = 9.979° and 12.004° from the computations which agrees with the experimental results. As for the C_D, two experimental curves are included in the plot. In the experiment, the C_D was measured based on two different methods, which used the force balance and the momentum deficit methods with the total pressure measurements collected by a wake rake (wake survey method) [23]. Since our numerical setup uses the slip wall assumption for the wind tunnel walls, it is expected that the C_D from the computations should compare better with the C_D measured using the wake method instead of the force balance as the former is less affected by the corner flow effects that are missing in our simulations. From the plot of C_D, the computational results also show small grid sensitivities and have good agreements with the experimental values at angles of attack, $\alpha = 5.989°$, $7.988°$, and $9.979°$. At $\alpha = 12.004°$, there is a large discrepancy between the experimental C_D values measured using the force balance and the wake method. The large discontinuity at this angle in the wake method measurement suggests some uncertainties at this angle using the method. As can be seen, there is a large grid sensitivity for C_D but the numerical prediction improves when the grid is refined. The mean C_D computed with grid E agrees reasonably well with the experimental value using force balance barring the large fluctuation at this angle. As for the C_M, over-predictions can be observed at different angles of attack with different grids. However, as the grid is refined, there are improvements in C_M for $\alpha = 7.988°$, $9.979°$ and $12.004°$ generally. The improvement is the most prominent at $\alpha = 12.004°$. At this angle, simulations with both grids C and D predict mean C_M values that are both positive and are very close to each other, in contrast to the negative value from the experiment after the pitch-break. However, with the target mesh refinement near the streamwise ice in grid E, a very negative mean value for C_M, similar to the experimental result, is obtained to reproduce the pitch-break behaviour during stall. At $\alpha = 14.000°$, only one simulation was attempted using the coarse grid C. Nevertheless, the stall behaviour is already predicted quite well numerically and the numerical mean values compare reasonably well with the experimental results at this angle, barring the large time variations in these quantities.

The mean pressure coefficients, $C_p = 2(\overline{p} - p_\infty)/(\rho_\infty U_\infty^2)$, distributed on the surface of the ED1977 iced wing at all five angles of attack are shown in Figure 12, where $\overline{p}$ is the mean surface pressure. p_∞ and ρ_∞ are the freestream pressure and density targeted at the point probe upstream of the wing respectively. The time-averaging of the pressure coefficients are performed consistently with the aerodynamic coefficients for each case using the same sampling start time and time-averaging duration. In the wind tunnel tests, the model had a main chordwise row of pressure taps and a secondary chordwise row of pressure taps. The main and secondary chordwise rows are located at $y = 0.514853b$ and $y = 0.416530b$ respectively, where the side walls are at $y = 0$ and $y = b$. While the main chordwise row of pressure taps covers the whole chord, the secondary row only spans from $x = 0.1c$ to the trailing edge. We have chosen to plot the C_p at the mid-span location $y = 0.5b$ which is considered to be least affected by the side walls and are close to the main chordwise row. In the C_p plots, it can be seen that the curves along both main and secondary rows are essentially the same, except for $\alpha = 14.000°$, where small difference is shown from $x = 0.1c$ to $0.4c$. At the low angles of attack, $\alpha = 5.989°$, $7.988°$, and $9.979°$, the C_p curves from the simulations agree well generally with those from experiments despite some noisiness near the leading edge ice that can be improved with longer time-averaging. In the smooth regions, there are small over-predictions of 0.05 on both pressure and suction sides which may be due to uncertainties in the wind tunnel setup. In our simulations, the wind tunnel walls are assumed to be slip wall with constant cross-section while the actual wind tunnel walls have developed boundary layers and are slightly diverging. At $\alpha = 12.004°$, the C_p curves obtained with grids C and D are very close to each other but agree poorly with the experiment. The C_p values near the leading and the trailing edges are under-predicted and over-predicted respectively on the suction side, which indicates that the iced wing is not completely stalled, and hence the mean C_L and C_M are both largely over-predicted using these two grids. On the other hand, the C_p from grid E are much closer to the experimental values, except minor differences at the leading edge on the suction side. At $\alpha = 14.000°$, while the C_p computed with grid C agrees quite well with the experimental measurement on the pressure side, some degrees of under-prediction and over-prediction are seen near the leading and trailing edges respectively on the suction side and this explains the small under-prediction in mean C_L and slightly less negative mean C_M compared with the experimental results.

C. ED1978 Case

The time histories of the coefficients, C_L, C_D, and C_M, at different angles of attack from the simulations using grid D are shown in Figure 13. From the time histories, it can be seen that at the lower angles of attack, $\alpha = 2.000°$, $3.995°$, and $5.992°$, the aerodynamic coefficients are all statistically well converged after 15 CTUs. Time averaging is performed from the 30th CTU for these angle until the end of simulations at the 50th CTU. However, the aerodynamic coefficients have large fluctuations with a long period of ~ 14 CTUs at $\alpha = 7.996°$. Therefore, the simulation at this angle of attack is conducted until 200th CTU while the statistics are also collected from 30th CTU. This low-frequency fluctuations are also observed in the lattice–Boltzmann simulations of the same ED1978 case in [25] and WMLES of another horn ice case of the NACA23012 airfoil [13], as well as in the experiments of an airfoil with leading edge horn ice accretion [35]. Gurbacki and Bragg [35] suggest that the low-frequency fluctuations in aerodynamic coefficients are possibly caused by a flapping mode at the shear layer induced by the horn ice and using their definition of Strouhal

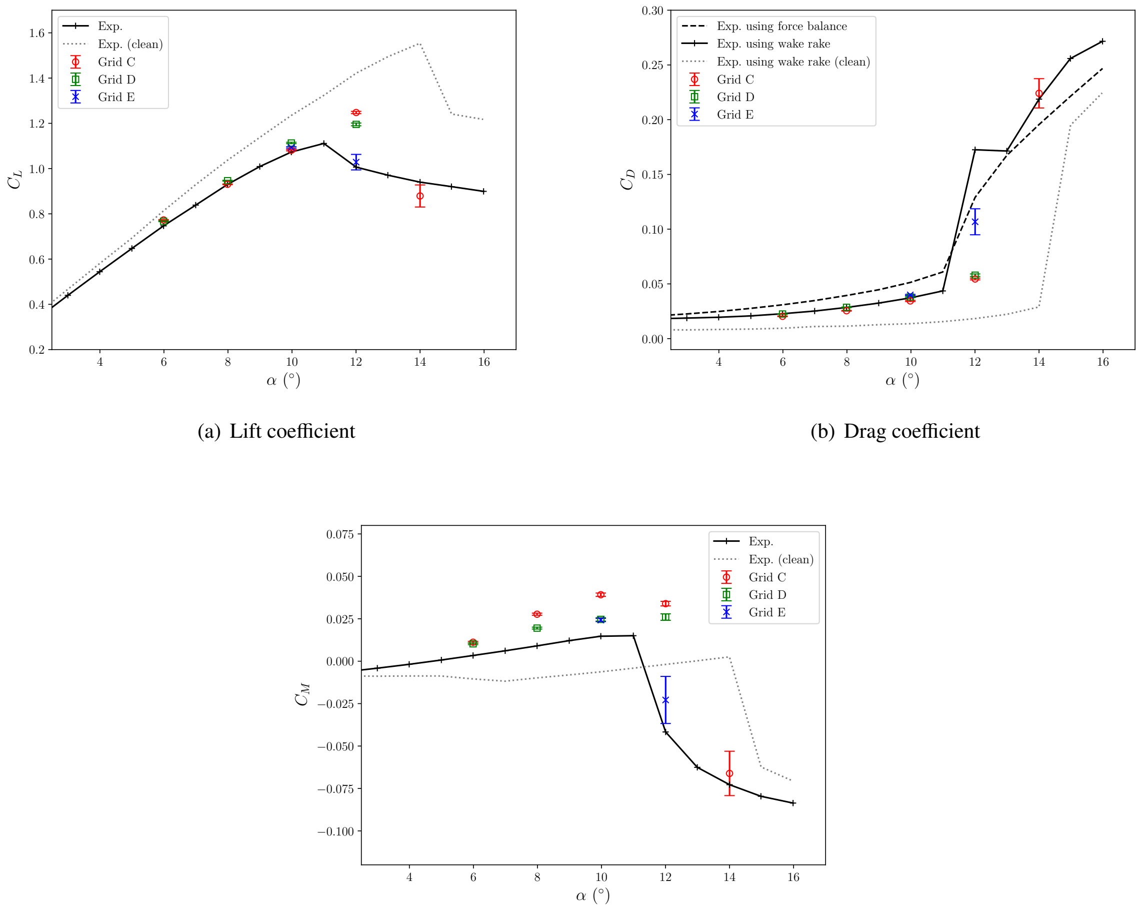

(a) Lift coefficient

(b) Drag coefficient

(c) Pitching moment coefficient

Fig. 11 Comparison of the lift, drag, and pitching moment coefficients from simulations with experimental results for the ED1977 case. Red circles: grid C; green squares: grid D; blue crosses: grid E; black solid line with pluses: experiment of the iced wing; gray dotted line: experiment of the clean wing. The error bars of the simulation results represent the RMSs of the fluctuations of the aerodynamic coefficients. The black dashed line: drag coefficient measured with the force balance; in contrast to using the momentum deficit method with the wake rake represented by the black solid line with pluses.

number, St, with projected height of the airfoil and freestream velocity magnitude (targeted at the point probe), we get $St \approx 0.01$ for the low-frequency mode, similar to values reported in other studies on airfoil with leading edge horn ice accretion [25, 35]. This peak St can also be seen in Figure 13(d) which shows the power spectral densities (PSDs) of C_L, C_D, and C_M at $\alpha = 7.996°$.

Figure 14 shows the comparison of the mean aerodynamic coefficients (with RMSs of the fluctuations) with the experimental results. The experimental results show that with the horn ice accretion, the iced wing has $C_{L,max} = 0.70$ and $\alpha_{stall} = 7.2°$. While it is not clear from the C_L plot, this α_{stall} was measured based upon the surface pressure distribution that showed a significant amount of lift generated on the forward portion of the airfoil section according to Broeren et al. [36]. The simulation results with both grids C and D have decent comparison with the experimental values at $\alpha = 2.000°$ and $3.995°$ with small over-predictions, and the grid sensitivities are small at these two angles. The mean C_L values are slightly over-predicted for both grids. While the mean C_D values obtained with grid C agree perfectly with the experimental values using the wake method, there are tiny under-predictions for the mean C_D values predicted using grid D. The mean C_M is slightly under-predicted and over-predicted at $\alpha = 2.000°$ and $3.995°$ respectively for

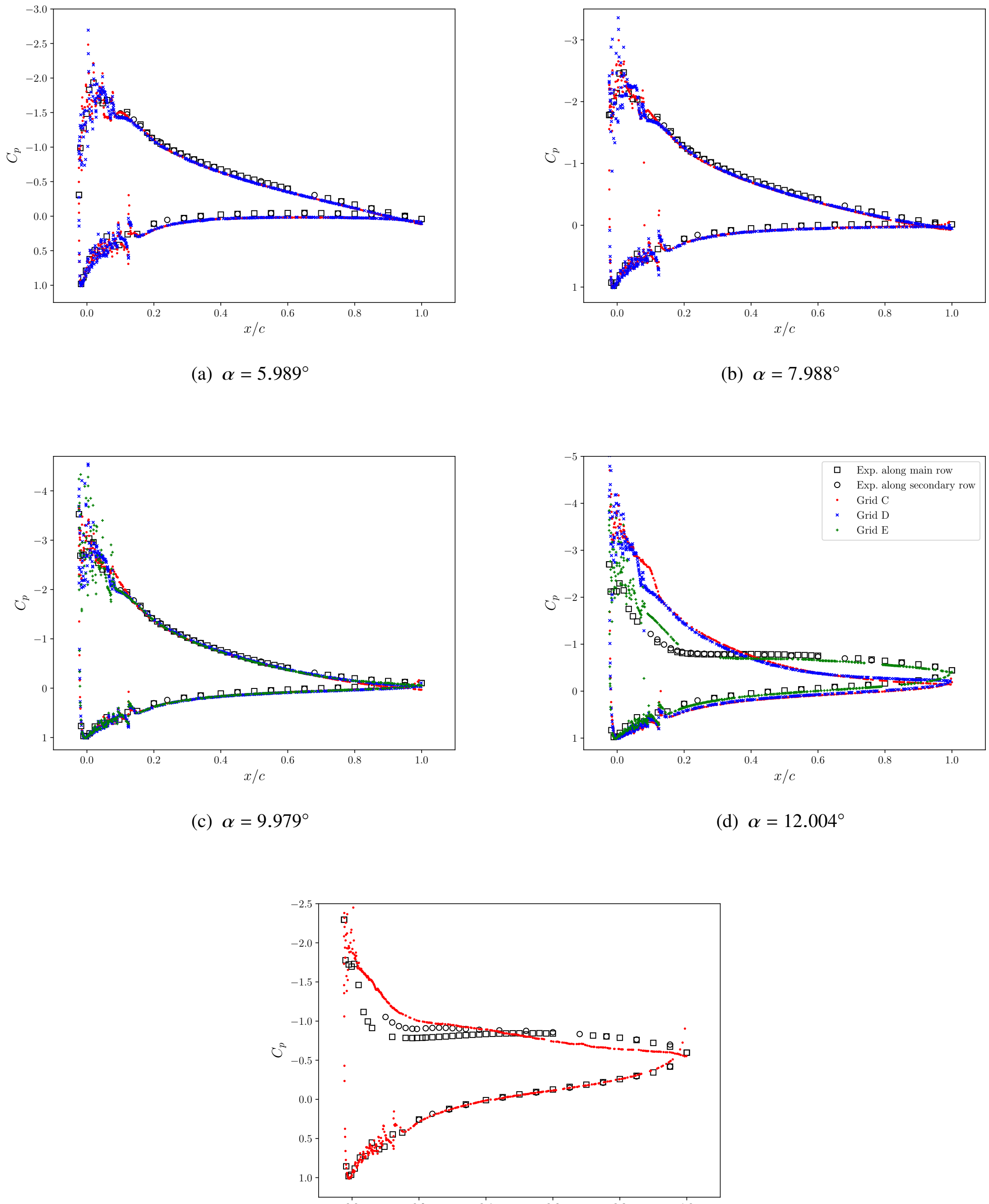

(a) α = 5.989°

(b) α = 7.988°

(c) α = 9.979°

(d) α = 12.004°

(e) α = 14.000°

Fig. 12 Comparison of the mean surface pressure coefficients, C_p, from simulations with experimental results at different angles of attack, α, for the ED1978 case. Red dots: grid C at mid-span; blue crosses: grid D at mid-span; green pluses: grid E at mid-span; black squares: experimental results along main row; black circles: experimental results along secondary row.

both grids. At α = 5.992°, the grid sensitivities are still small. Results with both grids show small over-predictions for both mean C_L and C_M and small under-predictions for mean C_D. At α = 7.996°, large RMSs in the fluctuations of aerodynamic coefficients can be seen from the simulation results, which are consistent with the low-frequency large-amplitude variations in the time histories of the aerodynamic coefficients. For the grid D, the RMSs of fluctuations of C_L, C_D, and C_M are 0.196, 0.0358, and 0.0481 respectively. The grid sensitivities in aerodynamic loads and pitching moment are also large, particularly for the latter. While mean C_L is slightly under-estimated, mean C_D and C_M are largely under-predicted and over-predicted for grid C. When the mesh is improved to grid D, the mean C_L becomes slightly over-predicted but the mean C_D and C_M agrees very well with the experimental measurements. Overall, the break in C_M at α = 6.2° is reasonably captured in the simulations.

The comparison of the time-averaged pressure coefficients, C_p, at the four different angles of attack is shown in Figure 15. Similar to the ED1977 streamwise ice case, there are also C_p measurements along the main and secondary chordwise rows for this ED1978 horn ice case. Again, we have chosen the mid-span to be the C_p cut location for our simulation results. At the lower angles of attack, α = 2.000°, 3.995° and 5.992°, the results are not quite sensitive with the grids, except at the leading edge horn ice. When the grid C is refined in regions near the leading edge to grid D, improvements in the C_p prediction are clearly observed. At α = 7.996°, while the C_p curve has tiny grid sensitivity on the pressure side except near the leading edge, the results computed using grid D agree much better with the experimental results on the entire suction side. Overall, the under-predictions near the leading edge and the over-predictions in the smooth regions on the suction side are largely eliminated when the grid is improved and this explains the improvement in mean C_M prediction from grid C to grid D at this angle. It should be noted that there are again small over-predictions of around 0.05 on both pressure and suction sides for most of these angles ($\approx$ 0.07 at α = 5.992°) in these simulation results, which are similar to the streamwise ice case due to uncertainties in reproducing the wind tunnel setup.

V. Concluding Remarks

The computational WMLES results of iced straight wings with two very different types of 3D leading edge ice accretion, streamwise ice and horn ice, using an octree Cartesian immersed boundary solver, Volcano ScaLES, were presented. These simulations were conducted with the full span wing in a wind tunnel setup such that the aerodynamic quantities form the computations can be directly compared to the uncorrected wind tunnel results with fewer uncertainties. In order to simulate the iced wings in the wind tunnel setup, precursor simulations using lower resolution grids were conducted to tune the back pressure such that the target freestream quantities were achieved at a point upstream of the wings. These precursor simulations also provide initial conditions for the higher resolution runs. In general, the aerodynamic loads and pitching moments obtained with these simulations have good comparison with the experimental measurements when sufficient grid resolution is used, particularly near the leading edge. While the lower two resolution grids cannot predict a complete stall state at $\alpha \approx 12°$, with higher resolution cells deployed near the leading edge, the stall behaviour is reproduced to match with the experimental aerodynamic results including the pressure coefficient. Similarly for the horn ice case, we found that local mesh refinement near the leading edge horn ice and the shear layers provides better aerodynamics predictions, because many physical phenomena near the leading edge, such as the laminar-turbulent transition at the shear layers and the reattachment of the separation bubbles are better captured. At $\alpha \approx 8°$, a low-frequency mode was seen in the WMLES which agrees with the observations in previous numerical and experimental studies of iced airfoils/wings with horn ice at high angles of attack.

Overall, these WMLES results show that the octree Cartesian immersed boundary solver is capable of predicting the iced aerodynamics of straight wings or airfoils with very complex and different 3D ice accretion at the leading edges. In addition, these high-resolution WMLES could be simulated in hours or days on desktop-like machines with only a few GPUs because of the highly memory-efficient implementation of the Cartesian methods in the CFD solver. It is expected that this scale-resolving Cartesian methodology, without any labor-intensive grid generation process, can be used for high-fidelity simulations of more complex iced aerodynamic devices, or even full aircraft configurations with ice accretion.

Acknowledgments

We would like to thank Dr. Andy P. Broeren from NASA Glenn Research Center for providing the laser-scanned geometries and experimental data of the 3D iced straight wings with the NACA 23012 airfoil section. We would like to thank Dr. Oliver M. Browne for the valuable discussion on the setup of the scale-resolving simulations.

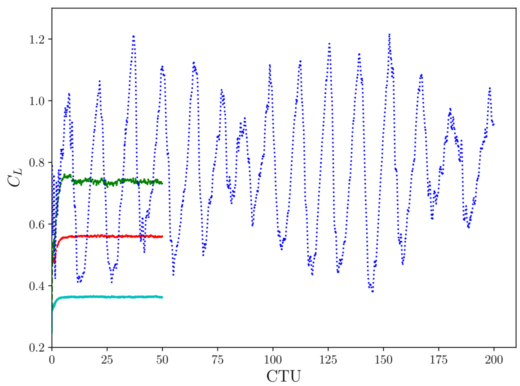

(a) Lift coefficient

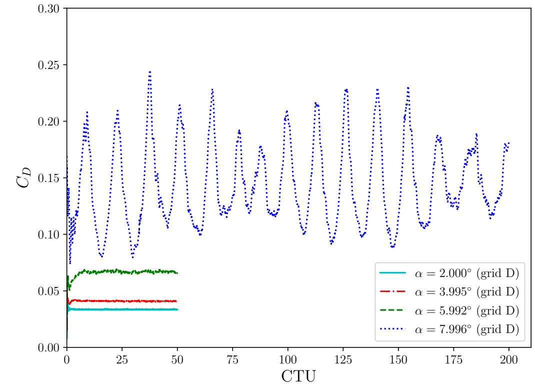

(b) Drag coefficient

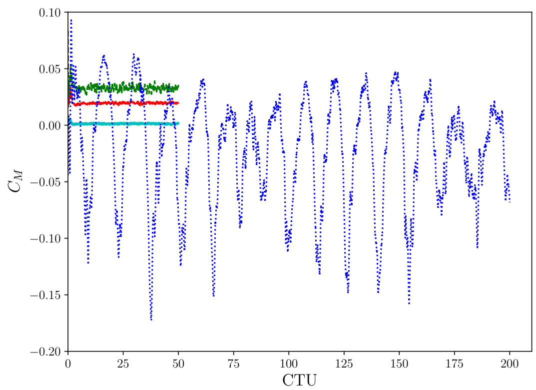

(c) Pitching moment coefficient

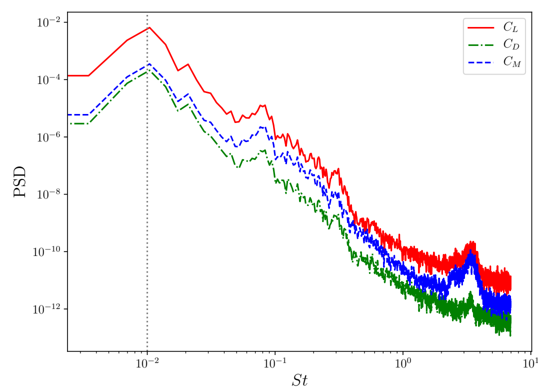

(d) PSD of time histories at $\alpha = 7.996°$ with grid D

Fig. 13 Time histories of the lift, drag, and pitching moment coefficients from the simulations at different angles of attack, α, for the ED1978 case, where cyan solid line: $\alpha = 2.000°$ with grid D; red dash-dotted line: $\alpha = 3.995°$ with grid D; green dashed line: $\alpha = 5.992°$ with grid D; blue dotted line: $\alpha = 7.996°$ with grid D.
The bottom right plot shows the power spectral density (PSD) of each aerodynamic coefficients at $\alpha = 7.996°$ with grid D, where red solid line: lift coefficient; green dash-dotted line: drag coefficient; blue dashed line: pitching moment coefficient. The vertical gray dotted line is at Strouhal number, $St = f \cdot c\ sin(\alpha)/U_\infty = 0.01$. The PSDs are computed using Welch's method with 75% overlap and Hann windowing for truncated time signals from the 30th to 200th CTU, where each truncated segment of signal has a bin width of 40 CTUs.

References

[1] Kwon, O., and Sankar, L., "Numerical study of the effects of icing on finite wing aerodynamics," *28th Aerospace Sciences Meeting*, 1990, p. 757.

[2] Bragg, M., Khodadoust, A., Soltani, R., Wells, S., and Kerho, M., "Aerodynamic measurements on a finite wing with simulated ice," *9th Applied Aerodynamics Conference*, 1991, p. 3217.

[3] Chung, J., and Addy, H., Jr, "A numerical evaluation of icing effects on a natural laminar flow airfoil," *38th Aerospace Sciences Meeting and Exhibit*, 2000, p. 96.

[4] Pan, J., and Loth, E., "Reynolds-averaged Navier-Stokes simulations of airfoils and wings with ice shapes," *Journal of aircraft*, Vol. 41, No. 4, 2004, pp. 879–891.

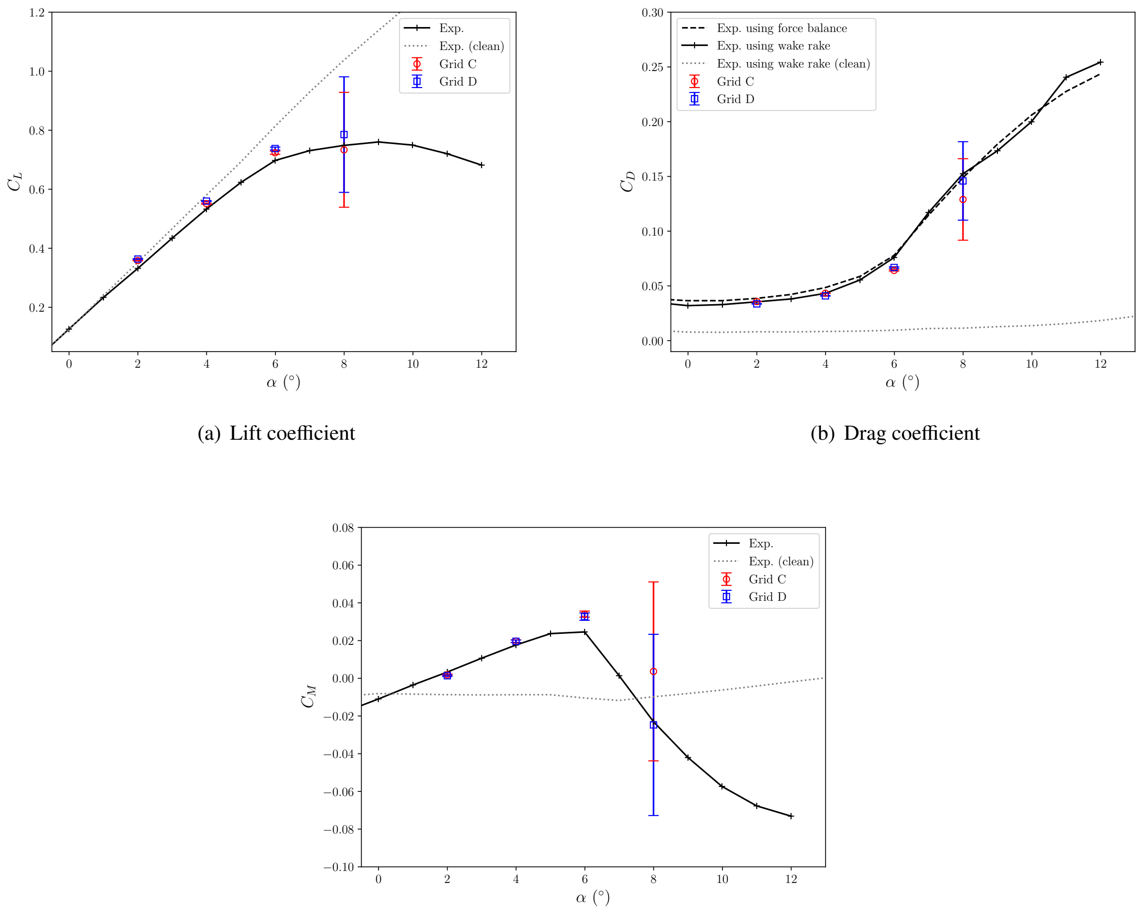

(a) Lift coefficient

(b) Drag coefficient

(c) Pitching moment coefficient

Fig. 14 Comparison of the lift, drag, and pitching moment coefficients from simulations with experimental results for the ED1978 case. Red circles: grid C; blue squares: grid D; black solid line with pluses: experiment of the iced wing; gray dotted line: experiment of the clean wing. The error bars of the simulation results represent the RMSs of the fluctuations of the aerodynamic coefficients. The black dashed line: drag coefficient measured with the force balance; in contrast to using the momentum deficit method with the wake rake represented by the black solid line with pluses.

[5] Cao, Y., Chen, K., and Sheridan, J., "Flowfield simulation and aerodynamic performance analysis of complex iced aerofoils with hybrid multi-block grid," *Proceedings of the Institution of Mechanical Engineers, Part G: Journal of Aerospace Engineering*, Vol. 222, No. 3, 2008, pp. 417–422.

[6] Pan, J., and Loth, E., "Detached eddy simulations for iced airfoils," *Journal of aircraft*, Vol. 42, No. 6, 2005, pp. 1452–1461.

[7] Mogili, P., Thompson, D., Choo, Y., and Addy, H., "RANS and DES Computations for a Wing with Ice Accretion," *43rd AIAA Aerospace Sciences Meeting and Exhibit*, 2005, p. 1372.

[8] Lorenzo, A., Valero, E., and De-Pablo, V., "DES/DDES post-stall study with iced airfoil," *49th AIAA aerospace sciences meeting including the new horizons forum and aerospace exposition*, 2011, p. 1103.

[9] Zhang, Y., Habashi, W. G., and Khurram, R. A., "Zonal detached-eddy simulation of turbulent unsteady flow over iced airfoils," *Journal of Aircraft*, Vol. 53, No. 1, 2016, pp. 168–181.

[10] Alam, M., Thompson, D. S., and Walters, D. K., "Hybrid Reynolds-Averaged Navier–Stokes/Large-Eddy simulation models for flow around an iced wing," *Journal of aircraft*, Vol. 52, No. 1, 2015, pp. 244–256.

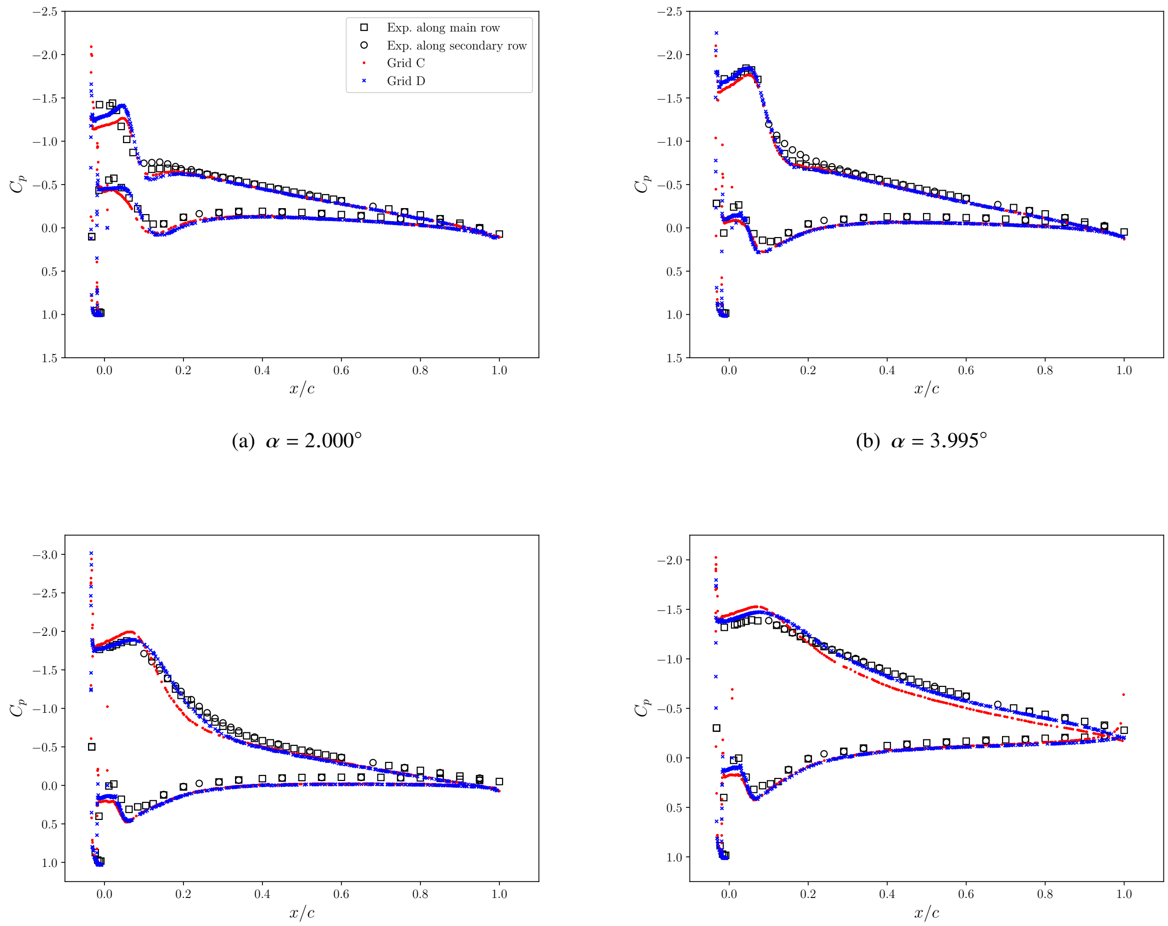

(a) $\alpha = 2.000°$

(b) $\alpha = 3.995°$

(c) $\alpha = 5.992°$

(d) $\alpha = 7.996°$

Fig. 15 Comparison of the mean surface pressure coefficients, C_p, from simulations with experimental results at different angles of attack, α, for the ED1978 case. Red dots: grid C at mid-span; blue crosses: grid D at mid-span; black squares: experimental results along main row; black circles: experimental results along secondary row.

[11] Xiao, M., Zhang, Y., and Zhou, F., "Numerical study of iced airfoils with horn features using large-eddy simulation," *Journal of Aircraft*, Vol. 56, No. 1, 2019, pp. 94–107.

[12] Xiao, M., Zhang, Y., and Zhou, F., "Numerical investigation of the unsteady flow past an iced multi-element airfoil," *AIAA Journal*, Vol. 58, No. 9, 2020, pp. 3848–3862.

[13] Wong, M. L., Ghate, A. S., Stich, G.-D., Kenway, G. K., and Kiris, C. C., "Numerical study on the aerodynamics of an iced airfoil with scale-resolving simulations," *AIAA SCITECH 2023 Forum*, 2023, p. 0252.

[14] Bornhoft, B., Jain, S. S., Goc, K., Bose, S. T., and Moin, P., "Large-eddy simulations of the NACA23012 airfoil with laser-scanned ice shapes," *Aerospace Science and Technology*, 2024, p. 108957.

[15] Larsson, J., Kawai, S., Bodart, J., and Bermejo-Moreno, I., "Large eddy simulation with modeled wall-stress: recent progress and future directions," *Mechanical Engineering Reviews*, Vol. 3, No. 1, 2016, pp. 15–00418.

[16] Stebbins, S. J., Loth, E., Broeren, A. P., and Potapczuk, M., "Review of computational methods for aerodynamic analysis of iced lifting surfaces," *Progress in Aerospace Sciences*, Vol. 111, 2019, p. 100583.

[17] Leary, W. M., *We Freeze to Please: A History of NASA's Icing Research Tunnel and the Quest for Flight Safety*, Vol. 4226, National Aeronautics and Space Administration, 2002.

[18] Addy, H. E., *Ice accretions and icing effects for modern airfoils*, National Aeronautics Administration, Glenn Research Center, 2000.

[19] Addy, H., Broeren, A., Zoeckler, J., and Lee, S., "A wind tunnel study of icing effects on a business jet airfoil," *41st Aerospace Sciences Meeting and Exhibit*, 2003, p. 727.

[20] Bragg, M., Broeren, A., Addy, H., Potapczuk, M., Guffond, D., and Montreuil, E., "Airfoil ice-accretion aerodynamic simulation," *45th AIAA Aerospace Sciences Meeting and Exhibit*, 2007, p. 85.

[21] Broeren, A. P., Bragg, M. B., Addy Jr, H. E., Lee, S., Moens, F., and Guffond, D., "Effect of high-fidelity ice-accretion simulations on full-scale airfoil performance," *Journal of aircraft*, Vol. 47, No. 1, 2010, pp. 240–254.

[22] Lee, S., Ratvasky, T., Thacker, M., and Barnhart, B., "Geometry and Reynolds-number scaling on an iced business-jet wing," *43rd AIAA Aerospace Sciences Meeting and Exhibit*, 2005, p. 1066.

[23] Broeren, A. P., Addy Jr, H. E., Lee, S., Monastero, M. C., and McClain, S. T., "Three-dimensional ice-accretion measurement methodology for experimental aerodynamic simulation," *Journal of Aircraft*, Vol. 55, No. 2, 2018, pp. 817–828.

[24] Lee, S., Broeren, A. P., Woodard, B., Lum, C. W., and Smith, T. G., "Comparison of Iced Aerodynamic Measurements on Swept Wing from Two Wind Tunnels," *2018 Atmospheric and Space Environments Conference*, 2018, p. 3493.

[25] König, B., Fares, E., and Broeren, A. P., "Lattice-Boltzmann analysis of three-dimensional ice shapes on a NACA 23012 airfoil," Tech. rep., SAE Technical Paper, 2015.

[26] Bragg, M. B., Broeren, A. P., and Blumenthal, L. A., "Iced-airfoil aerodynamics," *Progress in Aerospace Sciences*, Vol. 41, No. 5, 2005, pp. 323–362.

[27] Shu, C.-W., and Osher, S., "Efficient implementation of essentially non-oscillatory shock-capturing schemes, II," *Journal of Computational Physics*, Vol. 83, No. 1, 1989, pp. 32–78.

[28] Moin, P., Squires, K., Cabot, W., and Lee, S., "A dynamic subgrid-scale model for compressible turbulence and scalar transport," *Physics of Fluids A: Fluid Dynamics*, Vol. 3, No. 11, 1991, pp. 2746–2757.

[29] Lilly, D., "A proposed modification of the germano sugrid-scale closure method," *Phys Fluids A*, Vol. 4, 1992, pp. 633–635.

[30] Angel, J. B., Ghate, A. S., Kenway, G. K. W., Wong, M. L., Browne, O. M. F., and Kiris, C. C., "Validation of Immersed Boundary Wall-Modelled Large Eddy Simulations with F-16XL Flight Data," *AIAA Aviation 2024 Forum*, 2024.

[31] Angel, J. B., Ghate, A. S., Kenway, G. K. W., Wong, M. L., and Kiris, C. C., "Immersed Boundary Wall-Modelled Large Eddy Simulations for Automotive Aerodynamics," *AIAA Aviation 2024 Forum*, 2024.

[32] Wong, M. L., Ghate, A. S., Kenway, G. K. W., Angel, J. B., and Kiris, C. C., "Immersed Boundary Wall-Modelled Large Eddy Simulations of Subsonic Jet Flows and Acoustics," *AIAA Aviation 2024 Forum*, 2024.

[33] Wong, M. L., Ghate, A. S., Kenway, G. K. W., Angel, J. B., and Kiris, C. C., "Immersed Boundary Wall-Modelled Large Eddy Simulations of a Nose Landing Gear for Aeroacoustics," *AIAA Aviation 2024 Forum*, 2024.

[34] Kenway, G. K. W., Ghate, A. S., Browne, O. M. F., Wong, M. L., Angel, J. B., and Kiris, C. C., "Immersed Boundary Wall-Modelled Large Eddy Simulations of a Generic Hammerhead Payload Fairing," *AIAA Aviation 2024 Forum*, 2024.

[35] Gurbacki, H., and Bragg, M., "Unsteady flowfield about an iced airfoil," *42nd AIAA aerospace sciences meeting and exhibit*, 2004, p. 562.

[36] Broeren, A. P., Addy, H. E., Lee, S., and Monastero, M. C., "Validation of 3-D ice accretion measurement methodology for experimental aerodynamic simulation," *6th AIAA Atmospheric and space environments conference*, 2014, p. 2614.